ADVANCED FUNCTIONAL MATERIALS
www.afm-journal.de

Check for updates

Multimodal Characterization of Crystal Structure and Formation in Rubrene Thin Films Reveals Erasure of Orientational Discontinuities

*Jenna A. Tan, Jordan T. Dull, Steven E. Zeltmann, Jakhangirkhodja A. Tulyagankhodjaev, Holly M. Johnson, Alex Liebman-Peláez, Brendan D. Folie, Sven A. Dönges, Omar Khatib, Jonathan G. Raybin, Trevor D. Roberts, Leo M. Hamerlynck, Christian P. N. Tanner, Jina Lee, Colin Ophus, Karen C. Bustillo, Markus B. Raschke, Hendrik Ohldag, Andrew M. Minor, Barry P. Rand, and Naomi S. Ginsberg**

Multimodal multiscale characterization provide opportunities to study organic semiconducting thin films with multiple length scales, across multiple platforms, to elucidate crystallization mechanisms of the various microstructures that impact functionality. With polarized scanning transmission X-ray and 4D-scanning transmission electron microscopy, hybrid crystalline structures in rubrene thin films in which large crystalline domains surround a common nucleus and transition to a spherulite morphology at larger radii is observed. These high-resolution techniques reveal how azimuthal orientational discontinuities at smaller radii are erased as spherulite morphology takes hold. In situ crystallization in the films with optical microscopy is also captured, discovering the importance of considering the initial temperature increase of a film during thermal annealing over the crystallization timescale. This kinetic information of the radial crystallization rate and of corresponding film heating kinetics is used to estimate the temperature at which the larger crystalline regions transition into a spherulite. By combining the results obtained from the different characterization modes, it is learned that thermal conditions can sensitively affect the crystallization of rubrene and other organic thin films. The observations suggest opportunities for more complex temperature-dependent processing to maximize hybrid structures' functionality in organic thin films and demonstrate that multimodal studies deepen the understanding of structure-function dynamics.

1. Introduction

Organic semiconductor films can form a variety of microstructures that facilitate or inhibit electronic device functionality. For example, disordered grain boundaries in polycrystalline films and high-angle molecular orientation mismatch at such boundaries often correlate to poorer charge transport in thin film transistor geometries.[1–3] Processing-structure studies[4] provide guidelines for tuning structural order such as molecular orientation and crystalline grain size.[5] These studies are most effective at achieving a desired microstructure when both control of processing conditions and an understanding of the microstructure formation process can be developed.

Rubrene has one of the highest charge carrier mobilities of organic semiconductors at 20 $cm^2\ V^{-1}\ s^{-1}$ in single crystal form and has been extensively studied for thin film applications.[6,7] Depending on annealing conditions of an initially

J. A. Tan, J. G. Raybin, T. D. Roberts, L. M. Hamerlynck, C. P. N. Tanner, N. S. Ginsberg
Department of Chemistry
University of California
Berkeley, CA 94720, USA
E-mail: nsginsberg@berkeley.edu

The ORCID identification number(s) for the author(s) of this article can be found under https://doi.org/10.1002/adfm.202207867.

[+]Present address: Department of Chemistry, Columbia University, New York 10027, USA

[++]Present address: Citrine Informatics, Redwood City, CA 94063, USA

[+++]Present address: Advanced Conductor Technologies, Boulder, CO 80301, USA

[++++]Present address: Department of Electrical and Computer Engineering, Duke University, Durham, North Carolina 27708, USA

DOI: 10.1002/adfm.202207867

J. A. Tan, S. E. Zeltmann, J. A. Tulyagankhodjaev,[+] S. A. Dönges,[+++] O. Khatib,[++++] J. G. Raybin, T. D. Roberts, L. M. Hamerlynck, C. P. N. Tanner, J. Lee, M. B. Raschke, A. M. Minor, N. S. Ginsberg
NSF Science & Technology Center
STROBE
Berkeley, CA 94720, USA

J. T. Dull, H. M. Johnson, B. P. Rand
Department of Electrical and Computer Engineering
Princeton University
Princeton, NJ 08544, USA

S. E. Zeltmann, A. M. Minor
Department of Materials Science and Engineering
University of California
Berkeley, CA 94720, USA

J. A. Tulyagankhodjaev
Department of Chemistry
University of California
Los Angeles, CA 90095, USA

 © 2023 Wiley-VCH GmbH

deposited amorphous film, rubrene can crystallize into different morphologies. At lower temperatures rubrene forms platelets, a collection of larger single-crystalline domains characterized by their wedge shapes that share a common nucleus, as shown in **Figure 1**a. At higher temperatures rubrene crystallizes into spherulites, polycrystalline macrostructures (Figure 1b), whose many nanoscale crystallites are ordered with their orthorhombic *b*-axes pointing outward from a single nucleus, so that the crystal orientation gradually rotates about the nucleus. The electronic functionality of rubrene and other thin film organic semiconductors depends strongly on the structure at multiple length scales. Deterministically relating bulk outcomes like charge transport to microstructures such as platelets and spherulites ultimately requires structural characterization at multiple scales and proper correlation of the obtained characteristics.

Unfortunately, fully characterizing organic thin film microstructure and its formation is challenging precisely because it involves multiple characteristic scales, which would invoke multiple different techniques that need to be referenced to one another. Microstructural characterization of complex polycrystalline structures can involve techniques that span infrared to X-ray photons or employ scanning probe or electron capabilities.[8,9] For example, polarized optical microscopy (POM), as shown in Figure 1a,b, offers qualitative visualization of crystalline films on the tens to hundreds of micron length scales. Viewing films through crossed polarizers provides indirect orientation information through variations in intensity hues and is an accessible and non-destructive characterization

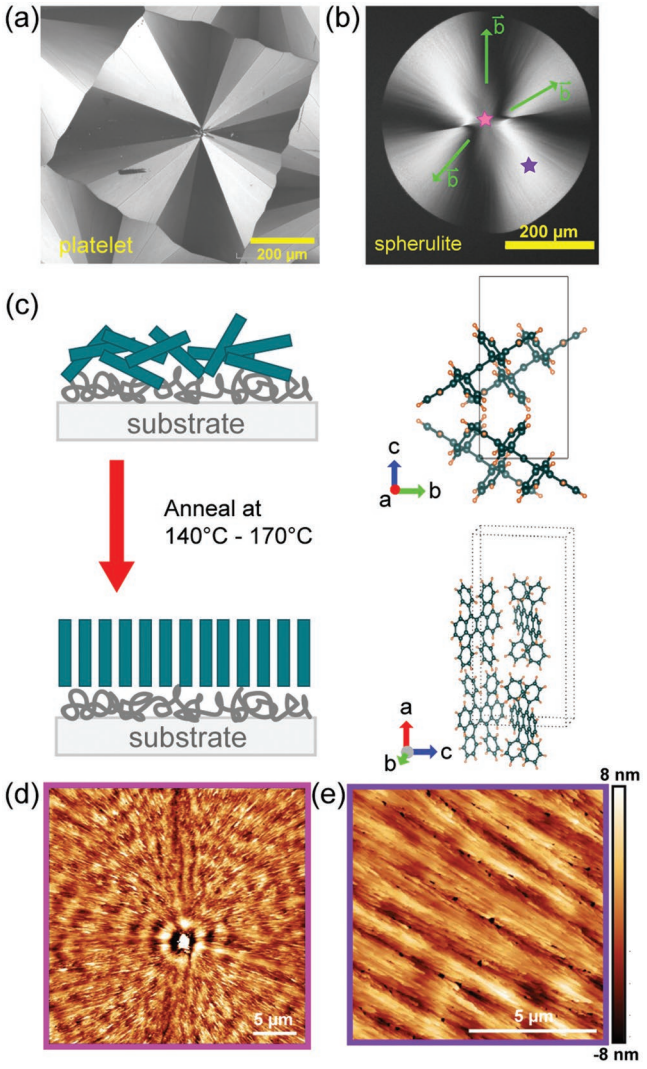

Figure 1. Crystallized rubrene thin film characterization. Polarized optical microscope images of a representative crystalline rubrene a) platelet and b) spherulite on glass/ITO substrates. c) Illustration of the annealing process for rubrene thin films. A 40 nm film of amorphous rubrene (represented by blue rectangles) on top of 5 nm of TPTPA (gray underlayer atop substrate) is annealed with setpoints in the 140–170 °C range to yield crystalline rubrene, as depicted by the upright blue rectangles. The orthorhombic crystal structure is shown from the in-plane perspective (*c*- and *b*-axes) and out-of-plane perspective (*a*-axis normal to the film). The green arrows shown in (b) represent the crystalline growth direction of orthorhombic rubrene. Representative AFM images for the surface morphology around d) the center of a spherulite indicated by the pink star in (b) and (e) the body of a spherulite indicated by the purple star in (b).

A. Liebman-Peláez, B. D. Folie[++] N. S. Ginsberg
Department of Physics
University of California
Berkeley, CA 94720, USA

S. A. Dönges, O. Khatib, M. B. Raschke
Department of Physics and JILA
University of Colorado
Boulder, CO 80309, USA

J. Lee
Division of Geological and Planetary Sciences
California Institute of Technology
Pasadena, CA 91125, USA

C. Ophus, K. C. Bustillo, A. M. Minor
National Center for Electron Microscopy
Molecular Foundry
Lawrence Berkeley National Laboratory
Berkeley, CA 94720, USA

H. Ohldag
Advanced Light Source
Lawrence Berkeley National Laboratory
Berkeley, CA 94720, USA

H. Ohldag
Department of Material Sciences and Engineering
Stanford University
Stanford, CA 94305, USA

H. Ohldag
Department of Physics
University of California Santa Cruz
Santa Cruz, CA 94064, USA

B. P. Rand
Andlinger Center for Energy and the Environment
Princeton University
Princeton, NJ 08544, USA

N. S. Ginsberg
Materials Science Division
Lawrence Berkeley National Laboratory
Berkeley, CA 94720, USA

N. S. Ginsberg
Molecular Biophysics and Integrated Bioimaging Division
Lawrence Berkeley National Laboratory
Berkeley, CA 94720, USA

N. S. Ginsberg
Kavli Energy Nano Science Institute
Berkeley, CA 94720, USA

© 2023 Wiley-VCH GmbH

16163028, 2023, 13, Downloaded from https://onlinelibrary.wiley.com/doi/10.1002/adfm.202207867 by University Of Colorado Librari, Wiley Online Library on [09/06/2023]. See the Terms and Conditions (https://onlinelibrary.wiley.com/terms-and-conditions) on Wiley Online Library for rules of use; OA articles are governed by the applicable Creative Commons License

16163028, 2023, 13, Downloaded from https://onlinelibrary.wiley.com/doi/10.1002/adfm.202207867 by University Of Colorado Librari, Wiley Online Library on [09/06/2023]. See the Terms and Conditions (https://onlinelibrary.wiley.com/terms-and-conditions) on Wiley Online Library for rules of use; OA articles are governed by the applicable Creative Commons License

technique. In addition to capturing static images of films, POM can also record the evolution of structure in films at the macroscopic level, for example, in situ during film processing.

Polarized scanning transmission X-ray microscopy (STXM) generates elemental composition maps based on the transmission of the focused polarized X-ray beam through a rastered sample. Generally, STXM offers sub-micron to tens of nanometer resolution, where the X-ray probe size is on average 50–100 nm but can achieve down to 25 nm resolution depending on the zone plate used.[10] By imaging the same region in a crystalline film with different X-ray polarizations, it is possible to also acquire a local crystal orientation map with polarized STXM. Polarized STXM provides nanoscale morphological characterization that is also sensitive to the electronic and chemical structure of the material.[11–13]

Conventional transmission electron microscopy (TEM) produces an image on a pixelated detector with an electron beam that passes through the sample with potentially higher resolution than optical microscopy and STXM. An electron diffraction pattern acquired from a region within the sample elucidates crystal structure.[14] 4D scanning TEM (4D-STEM) builds upon standard TEM by measuring a full diffraction pattern at each point in a sample using a scanning electron probe that is 0.5–50 nm in diameter. By comparing each diffraction pattern to a library of templates, the orientation of a crystalline grain can be calculated and mapped onto its respective field of view.[15] 4D-STEM quantitatively uncovers defects or anomalies in crystal structure packing and orientation.[16,17]

Despite the complementary scales and value of accessing information from each of these forms of imaging, combining the information self-consistently has remained challenging. The most significant barriers revolve around correlating sample measurements across modalities and developing the resultant data analysis workflow, which includes co-registering measurements, relating different spatial regions across measurements, and processing data across different dimensions.[18] Organic films, as relatively soft materials, are particularly susceptible to damage or irreversible chemical change and require a non-trivial investment in optimizing acquisition parameters to avoid sample destruction, especially with X-ray and electron microscopies. Furthermore, each technique typically requires different substrates or film thicknesses that must be accommodated self-consistently in order to correlate each form of image acquired to the others.

In spite of these challenges, we use multimodal characterization spanning micron and nanometer length scales to identify a hybrid microstructure in rubrene thin films, where large crystalline platelet domains radially transition into a spherulite morphology. We use X-ray and electron microscopies to image and quantify the disappearance of orientational discontinuities between platelet domains as the microstructure transitions into a spherulite morphology at two different scales. We also use polarized optical microscopy to capture the in situ crystallization process, and extract the associated kinetics, which enables us to estimate the temperature at which this transition occurs. Our multimodal imaging approach relies on a robust thin film processing protocol, using POM for initial characterization, and optimal, minimally destructive electron and X-ray acquisition parameters. For example, recent efforts to determine such parameters has made it possible to characterize organic films in detail with 4D-STEM through sample cooling and minimizing beam dose.[16,17] Multimodal characterization enables us to attribute the observed hybrid microstructure to sufficiently slow substrate thermalization that allows for crystallization to proceed through multiple morphologies. We furthermore demonstrate how such hybrid microstructures can form during annealing in other organic semiconductor thin films, suggesting that our findings from the detailed study of rubrene translate to various molecular systems and processing conditions. Our observations suggest that finely controlling microstructure also calls for advanced temperature control protocols.

2. Results and Discussion

Before discussing our correlative multimodal imaging of crystallized rubrene thin films via polarized STXM, 4D-STEM, and POM, we describe their preparation and pre-characterization. All samples are prepared by physical vapor deposition, first depositing a 5 nm tris(4-(5-phenylthiophen-2-yl)phenyl) amine (TPTPA) underlayer on the substrate, followed by 40 nm of amorphous rubrene. Amorphous samples are kept in a nitrogen-filled glovebox where they are also annealed on a preheated hotplate to crystallize rubrene as shown in Figure 1c (with the exception of the in situ optical experiments described below). This robust rubrene thin film processing protocol enables consistent crystallization across a variety of substrates, and previous research has determined that substrate choice does not impact rubrene crystallization on account of the TPTPA underlayer.[19,20] We use 10–200 nm SiN free-standing membrane substrates for electron and X-ray transparency in polarized STXM and 4D-STEM measurements, while glass substrates coated with indium tin oxide (ITO) are used in the in situ optical experiments for ease of encapsulation in order to anneal outside of the glovebox. Crystallizing rubrene directly atop of SiN substrates is especially helpful for TEM measurements since it bypasses the need to transfer the crystalline film between unlike substrates.

For pre-characterization, we use POM to confirm crystallization of thin films and map out areas of interest for STXM and 4D-STEM measurements. Its hundreds-of-micron-scale field-of-view enables quick identification of various regions of the spherulites and their locations relative to one another for the nano- and sub-nanoscale measurements. Under optical linear crossed-polarizers, spherulites exhibit smoothly varying azimuthal changes in contrast and a signature Maltese cross pattern (Figure 1b), representative of the correlation between the nanocrystallite *b*-axis and the spherulite radial vector. Grazing incidence wide-angle X-ray scattering (Figure S1, Supporting Information) confirms orthorhombic crystal structure (Figure 1c), which is the electronically relevant crystal structure for device applications, given that the π-stacking along the *b*-axis facilitates charge transport. A Scherrer analysis suggests the grains are elongated along this axis (Table S1 and related text, Supporting Information). Atomic force microscopy (AFM) images show nanoscale crystalline rods that have grown radially outward from the nucleus (Figure 1d) at the location indicated by the pink star in Figure 1b. The rod-like shape is consistent

 © 2023 Wiley-VCH GmbH

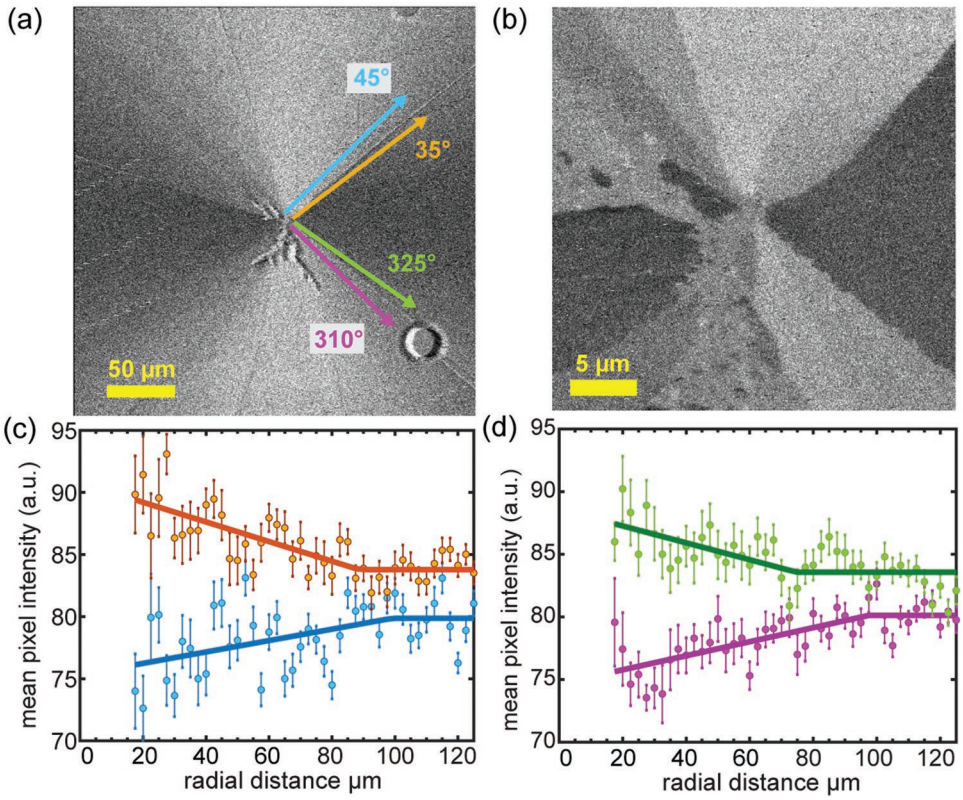

Figure 2. STXM imaging and analysis. a) Grayscale ratiometric STXM image of a spherulite annealed on a 200 nm SiN window at 170 °C for 1 min at a large field-of-view with 450 nm pixel resolution. b) A separate ratiometric STXM image of the same spherulite with 60 nm pixel resolution focused on the nucleus and emanating single-crystalline domains. c,d) Profiles of mean pixel intensity as a function of distance from the nucleus following two pairs of radial vectors, each surrounding a given orientational discontinuity. Colors of the intensity profiles correspond to the colored radial vectors in (a). Mean pixel intensities are shown as circles with their corresponding standard deviations shown as error bars, and the piecewise fit to the profiles are shown as solid lines. The fitting parameters are shared in Table 1.

with the higher crystallization rate along the *b*-axis and the Scherrer analysis.[20] Figure 1e shows similarly aligned rods further away from the nucleus at the location of the purple star in Figure 1b. To expand on the nanoscale information that AFM provides us, we also use infrared scattering scanning nearfield optical microscopy (IR *s*-SNOM) (Figures S2 and S3, Supporting Information) to probe the growth front to determine whether a signal could be distinguished between amorphous and crystalline rubrene.[21] Between crystalline and amorphous rubrene, the skeletal ring vibrations decreased in strength to the detection limit of the IR *s*-SNOM set-up over a distance of 700 nm. In the same region the disorder associated with this transition, as concluded from the increased spread in vibrational frequencies, also increased (Figure S3, Supporting Information). This suggests a lower limit of 700 nm for the width of crystalline growth front.

2.1. Polarized STXM reveals a hybrid crystalline microstructure

We begin describing our multimodal imaging of annealed rubrene thin films by focusing on polarized STXM with varying resolution and field-of-view. We imaged at 284.5 keV, which is close to the carbon K-edge (Figure S4, Supporting Information). An area of interest was first rastered with vertical polarization and next with horizontal polarization to obtain two distinct polarized images, each with high contrast. **Figure 2**a shows a 300 × 300 µm polarized STXM image of the center of an apparent spherulite. The image shown is a ratio of the images collected with vertical and horizontal polarizations to enhance the intensity contrast. The greyscale pixel intensity is a proxy for crystal orientation, where white pixels correspond to crystallites oriented parallel to the X-ray polarization, and black pixels correspond with crystallites oriented orthogonal to it.

We focus on a recurring motif characterized by an abrupt azimuthal change in transmission contrast observed next to the nucleus that gradually smooths out at larger radii. In a perfect spherulite the local crystal *b*-axis orientation would match that of a radial vector originating at the nucleus to generate a smoothly varying orientation distribution, as is apparent in Figure 1b. In polarized STXM, this would translate into smooth azimuthal changes in the greyscale pixel intensity. Instead, near the nucleus we observe sharp azimuthal changes in X-ray transmission between more uniform patches of transmission. Another higher-resolution ratiometric image centered at the same spherulite nucleus (Figure 2b) clearly demonstrates the sharp change in greyscale surrounding a nucleus, also suggesting platelet-like domains. With the larger field of view in Figure 2a, we observe these sharp changes disappear at larger radii. Consider for example the behavior as a function of

© 2023 Wiley-VCH GmbH

16163028, 2023, 13, Downloaded from https://onlinelibrary.wiley.com/doi/10.1002/adfm.202207867 by University Of Colorado Librari, Wiley Online Library on [09/06/2023]. See the Terms and Conditions (https://onlinelibrary.wiley.com/terms-and-conditions) on Wiley Online Library for rules of use; OA articles are governed by the applicable Creative Commons License

Table 1. Determination of the onset radius for the final crystal orientation of the platelet-to-spherulite transition and the corresponding temperature.

$\theta_{azimuthal}$	Onset radius of final $\theta_{crystal}$ (µm)	Final crystal orientation (θ)	Corresponding T with upper and lower bound (°C)
35°	80 ± 16	31 ± 4	134 (125, 138)
45°	99 ± 49	48 ± 6	136 (122, 146)
310°	98 ± 24	313 ± 4	136 (127, 142)
325°	75 ± 22	327 ± 3	133 (123, 138)

distance from the nucleus at ~40°. Tracing the orange and blue pair of radial vectors on each side (35° and 45°, respectively), the greyscale values gradually converge to those expected for a spherulite. Another example of this observation is highlighted by the pink and green pair of radial vectors at 310° and 325°.

To quantify this behavior, we analyze in Figure 2c,d the radial transmission profiles of horizontally polarized images by considering the X-ray transmission as a function of radial distance from the nucleus at the azimuthal angles on opposite sides of the two sharp changes in polarized X-ray transmission shown in Figure 2a. In both cases on both sides of the respective abrupt changes, we observe that the transmission evolves gradually from its greyscale value near the nucleus at small radii to a value beyond which it stabilizes within a certain radial range away from the nucleus. Next, we fit these radial profiles to a piecewise function to capture the approximate distance (X_1) from the nucleus at which the greyscale value stabilizes (Y_1):

$$\text{Intensity}\,(Y)=\begin{cases}\dfrac{Y_1-Y_0}{X_1}x+\left(Y_1-\dfrac{Y_1-Y_0}{X_1}X_1\right), x<X_1\\ Y_1, x\geq X_1\end{cases} \quad (1)$$

where Y_0 is the initial greyscale value. For example, in Figure 2c, the greyscale values that correspond to the 35° radial vector (orange) begin at ~90 at 20 µm from the nucleus and drop to ~84 about 80 µm from the nucleus, remaining at that value thereafter. To provide more physical context for this observation, we convert the greyscale value of transmission to crystal *b*-axis orientation through the sinusoidal relationship expected for smoothly varying intensity over 360°: $I = (I_{max} - I_{min})\sin^2(\theta_{crystal} + \phi) + I_{min}$ (Figure S6, Supporting Information). Therefore, in terms of local crystal *b*-axis orientation, in this example following the 35° radial vector, we find that beginning at the nucleus, the local *b*-axis orientation gradually and continually changes until it stabilizes at 31° ± 4° at 80 µm. A similar behavior is observed at the 45° radial vector (blue) on the opposite side of the abrupt change in transmission: the initial *b*-axis orientation is most disparate at smaller radii (~75° at 20 µm) and gradually changes to achieve a value of ~48° ± 6° around 100 µm, which is consistent with a smaller difference in orientation relative to the value at 45°. Related trends about 317.5° are plotted in green and magenta in Figure 2d, and all of the data are summarized in Table 1.

The plots of crystallite orientation versus distance from the nucleus obtained on opposite sides of the sharp change in transmission contrast suggest that abrupt transmission changes over small angular ranges correspond to an orientational discontinuity. The crystallites on either side of the discontinuity have uniform transmission contrast over a larger azimuthal range and orient independently of the direction of the radial vector. The onset radius at which the local crystallite orientation near a discontinuity begins to align with the radial vector ranges between 75 and 99 µm (Table 1). Although an improved signal-to-noise ratio in the image might enhance visualization of additional discontinuities possibly present in the spherulite, the two identified in Figure 2a and additional examples in Figure S7 (Supporting Information) suggest a consistent and reproducible trend.

2.2. 4D-STEM corroborates a hybrid crystalline microstructure

We use 4D-scanning transmission electron microscopy to obtain higher resolution orientation maps at the disappearance of an orientational discontinuity. We measured samples on a

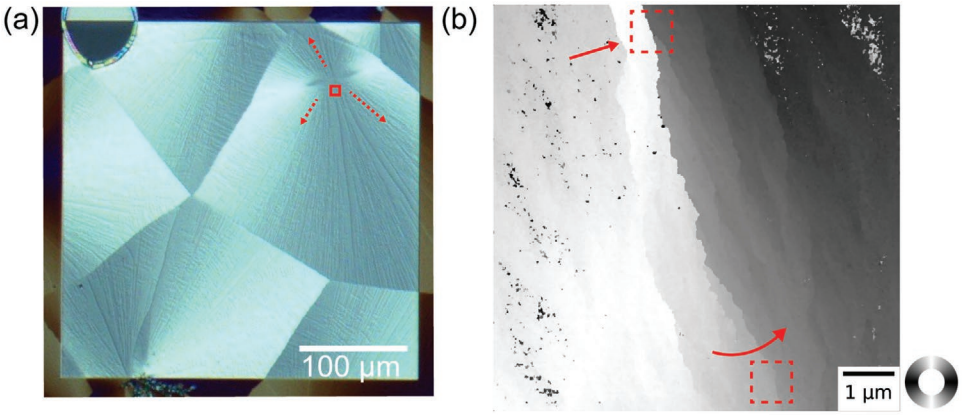

Figure 3. Orientational mapping by 4D-STEM. a) POM image of spherulites within the window region studied with 4D-STEM. The red box (8 × 8 µm) indicates a representative field of view shown in (b), and the red arrows pointing outward from the spherulite nucleus correspond to the local in-plane orthorhombic *b*-axis. b) In-plane *b*-axis orientation map where the greyscale indicates the orthorhombic *b*-axis orientation. The abrupt change in orientation observed at the top of the map (top arrow and box) is erased at greater distances from the nucleus, seen as a smooth change in orientation along the bottom of the map. The red boxes indicate areas visualized with Bragg vector maps in Figure S8 (Supporting Information).

© 2023 Wiley-VCH GmbH

16163028, 2023, 13, Downloaded from https://onlinelibrary.wiley.com/doi/10.1002/adfm.202207867 by University Of Colorado Librari, Wiley Online Library on [09/06/2023]. See the Terms and Conditions (https://onlinelibrary.wiley.com/terms-and-conditions) on Wiley Online Library for rules of use; OA articles are governed by the applicable Creative Commons License

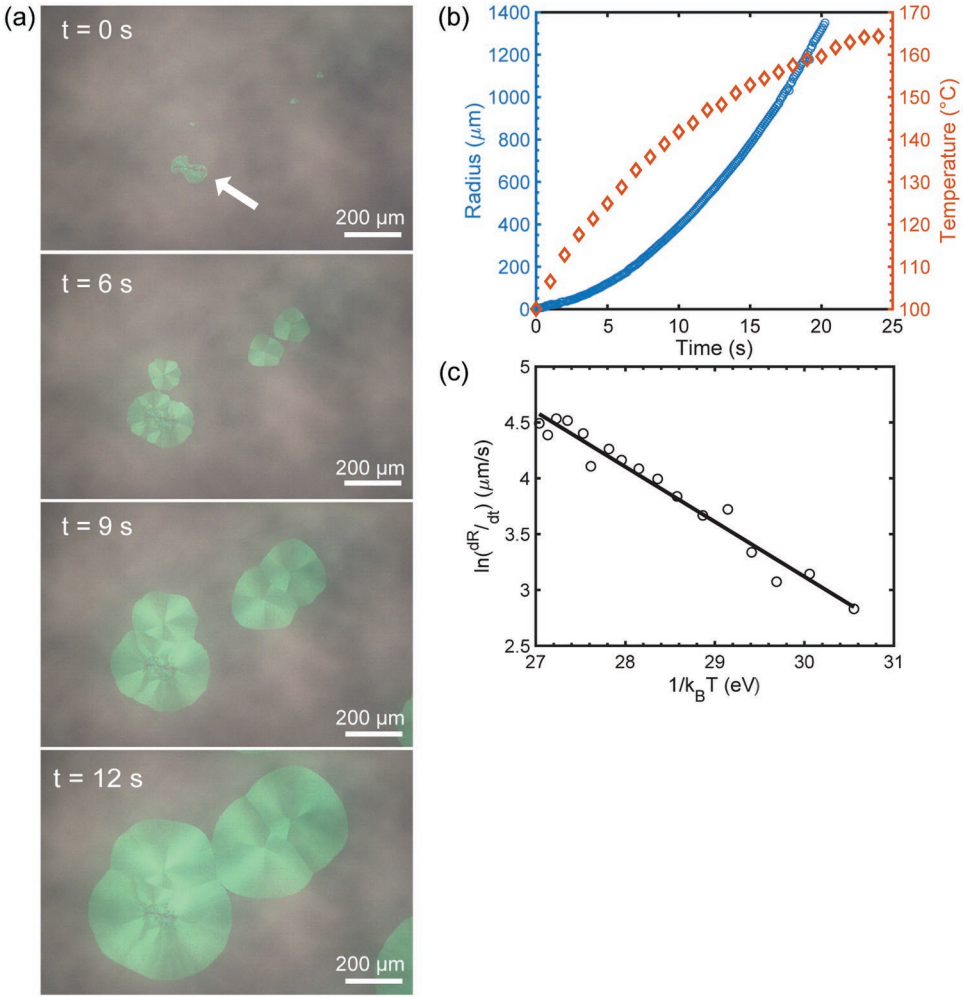

Figure 4. In situ rubrene crystallization. a) POM of in situ rubrene crystallization at 0, 6, 9, and 12 s on a glass/ITO substrate. b) The average radial growth of spherulites observed in POM shown in blue, and the glass/ITO substrate temperature rise to the ceramic heater plate setpoint in orange. c) The natural log of the spherulite growth rate as a function of the inverse temperature. A line with slope of −0.49 ± 0.02 eV fits the data, indicating Arrhenius behavior for crystallization.

10 nm thick SiN window, and the samples were kept at ~90 K during imaging to reduce damage caused by the electron beam. Given that spherulites are hundreds of micrometers in size and 4D-STEM has a limited field-of-view of less than 10 × 10 µm, preparatory identification of the apparent spherulites formed on the SiN window was essential. Polarized optical images of the films allow us to identify and characterize regions that represent the general feature of a spherulite, such as the nucleus, the main part of the spherulite body, and the growth front where crystallization was arrested.

We present the POM image of a crystallized rubrene film studied via 4D-STEM with the representative scan area indicated by a red box in **Figure 3**a. The area explored corresponds to a region a distance away from the nucleus of an apparent spherulite. We generate a quantitative orientation map of this region using a newly developed automated crystal orientation mapping procedure with an example shown in Figure 3b.[15,22] Briefly, a library of unique orthorhombic diffraction orientation patterns is simulated, and the experimentally acquired diffraction patterns are compared to this library. The experimental orientations are found through the maximum correlation value between the experimental diffraction pattern and the library pattern, where white corresponds to a vertical *b*-axis orientation.

The abrupt change in greyscale from light to dark observed across two grains at the top of Figure 3b marked by the arrow and box corresponds to an abrupt change in crystallite orientation of ~45°. This orientational discontinuity gives way at greater distances from the nucleus to more gradual azimuthal changes in local crystal orientation, moving smoothly from light to dark, indicated by the lower red arrow. This indicates that the *b*-axis crystal orientation continuously adjusts over at least 45° to maintain its orientation along the radial vector of the crystallized structure. We also visualize the relative degrees of misorientation described in the orientation map by compiling the diffraction patterns acquired from the scan into a Bragg vector map (Figure 3b red boxes, Figure S8, Supporting Information). The Bragg vector map associated with the upper box in Figure 3b shows an offset of ~45° in two distinct orthorhombic diffraction patterns, reflecting the orientational discontinuity. Further away from the discontinuity (lower box in Figure 3b)

© 2023 Wiley-VCH GmbH

16163028, 2023, 13, Downloaded from https://onlinelibrary.wiley.com/doi/10.1002/adfm.202207867 by University Of Colorado Librari, Wiley Online Library on [09/06/2023]. See the Terms and Conditions (https://onlinelibrary.wiley.com/terms-and-conditions) on Wiley Online Library for rules of use; OA articles are governed by the applicable Creative Commons License

the Bragg vector map shows a smearing of diffraction patterns, indicating in-plane rotation of the *b*-axis crystal orientation even over this small azimuthal range.

2.3. Heating and crystallization kinetics suggest origins of hybrid microstructure

To investigate the formation of the hybrid platelet-spherulite structure observed in STXM and 4D-STEM, we use POM to record a movie of the crystallization by thermally annealing amorphous rubrene films in situ. This process also allows us to extract the macroscopic crystallization kinetics of rubrene thin films. For these measurements, we encapsulated amorphous rubrene films, to avoid photo-oxidation, on a glass substrate coated with ITO and placed the sample on a layer of thermally conductive materials atop of a ceramic heater to facilitate annealing (Figure S9, Supporting Information). We set the ceramic heater temperature to 190°C to target spherulite growth upon annealing. This temperature ensured the highest fidelity of optical microscope data collection to the glovebox protocol used to fabricate the films used in X-ray and electron microscopies.

Movie frames representative of different stages of crystallization are shown in **Figure 4**a. The range of green shades corresponds to crystallized rubrene at different orientations. Most nuclei are too small to observe in optical microscopy, although the spherulite marked by a white arrow at $t = 0$ in Figure 4a has a sufficiently large nucleus that it is visible. This larger nucleus is visually consistent with rubrene's triclinic structure due to its distinct visual roughness in optical microscopy. Rubrene's triclinic structure forms at lower temperatures but orthorhombic rubrene can nucleate and crystallize from these triclinic structures.[20] We record crystallization until the spherulites impinge on each other, first seen ~9 s and seen even more prominently at 12 s (Figure 4a). In this measurement, the gradual change in color intensity we typically observe under crossed-polarizers is not sufficiently clear to directly discern platelet-like versus spherulite-like morphology, emphasizing the need for multimodal studies. Signs that indicate spherulite growth rather than platelet growth are the presence of a faint Maltese cross for all observable radii and the lack of any sharp azimuthal changes in green shades that would correspond to an intra-platelet grain boundary.

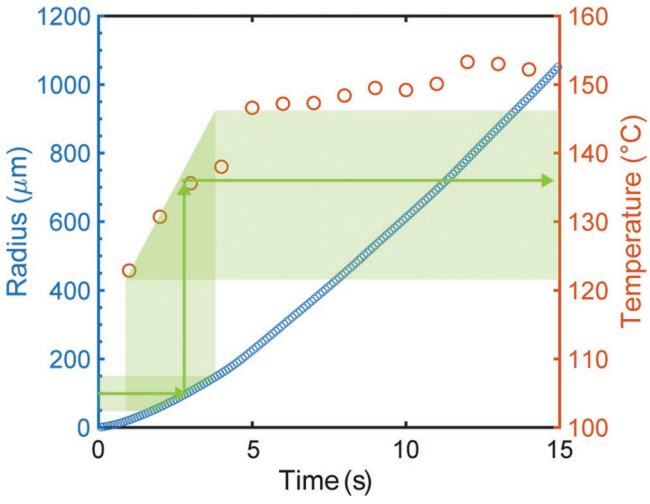

Figure 5. Predicted radial growth on a SiN window. The temperature vs. time of a 200 µm Si chip after being placed on a hotplate with a setpoint of 170°C (orange), and the expected spherulite radius on a SiN-on-Si substrate (blue) calculated using the Arrhenius parameters from the in situ POM experiment performed on glass/ITO. An example of mapping between radius and temperature is shown for the 45° radial vector from Figure 2d where the green bands map out a range of plausible values for the transition temperature.

The primary value of the ability to non-invasively image film crystallization however is that it allows us to track the value of the crystallized radius as a function of time, $R(T,t)$ (Figure 4b, blue) and to calculate the growth rate by taking its first derivative $\frac{dR}{dt}(T,t)$ (Figure S10, Supporting Information). Because it takes a finite time for the substrate to reach the heater plate set point, we are also able to calculate the activation energy for rubrene crystallization, under the assumption that the rubrene film remains in equilibrium with its immediate surroundings as it is being heated. We separately measure the glass substrate temperature increase toward the heater setpoint (Figure 4b, orange) so that it can be combined with dR/dt to obtain the growth rate versus temperature. Based on the glass substrate temperature measurement, we also infer that crystallization begins at 106°C. By measuring the glass substrate temperature rise, $T(t)$ (Figure 4b, orange), each $T(t)$ data point can be related back to the spherulite radius and corresponding growth rate at that same time point. Finally, we plot the natural log of growth rate $\ln(dR/dt)$ against inverse temperature and fit the data to a straight line (Figure 4c) to obtain an Arrhenius activation energy of −0.49 ± 0.02 eV. The straight line indicates that we are observing Arrhenius kinetics. Data for three spherulites captured in the movie are averaged to produce the Arrhenius plot shown in Figure 4c.

Although we calculate an activation energy from a different rubrene film thickness of 40 nm, we note our value of 0.49 eV is about three times smaller than previous measurement on glass/ITO substrates[20] and ~40% smaller than that measured on hexamethyldisilazane -functionalized SiO_2 substrates.[23] Thus, despite the challenge of comparing measurements in different configurations, we hypothesize that the inclusion of the underlayer drives a smaller activation energy for crystallization by acting as a mobile surface that facilitates exploration of the energetic landscape by rubrene molecules to crystallize.[19] The underlayer may also serve as a buffer against additional influence from the underlying substrate. Since we use the same 5 nm TPTPA underlayer for all rubrene films grown on glass/ITO or SiN substrates, we expect that the activation energy is likely similar for the glass and SiN substrates in this work.

Although the temperature of a SiN window is difficult to measure in situ while a rubrene film is being annealed for X-ray or electron imaging, we developed a strategy to estimate the temperature at which the larger platelet-like regions transition into a spherulite morphology observed in the polarized STXM and 4D-STEM images. To do so, we combine the Arrhenius kinetics information obtained from the in situ POM measurements with an estimate of the SiN substrate

© 2023 Wiley-VCH GmbH

16163028, 2023, 13, Downloaded from https://onlinelibrary.wiley.com/doi/10.1002/adfm.202207867 by University Of Colorado Librari, Wiley Online Library on [09/06/2023]. See the Terms and Conditions (https://onlinelibrary.wiley.com/terms-and-conditions) on Wiley Online Library for rules of use; OA articles are governed by the applicable Creative Commons License

16163028, 2023, 13, Downloaded from https://onlinelibrary.wiley.com/doi/10.1002/adfm.202207867 by University Of Colorado Librari, Wiley Online Library on [09/06/2023]. See the Terms and Conditions (https://onlinelibrary.wiley.com/terms-and-conditions) on Wiley Online Library for rules of use; OA articles are governed by the applicable Creative Commons License

thermalization as a function of time. To obtain this thermalization estimate, we measure the temperature rise as a function of time of a 200 µm Si chip after being placed on a 170°C hotplate (**Figure 5**, orange). Since the SiN window sits atop of a 200 µm Si frame, thermal transport through the Si frame, being 3 orders of magnitude thicker than the SiN, is the rate-limiting step to heat the organic film. In addition, lateral thermal transport in the SiN windows appears to be uniformly rapid enough to neglect for our estimate, given that the onset of crystallization is observed to be synchronous over the entire window area in addition to areas of the SiN backed directly by Si (Figure 3a; Figure S11, Supporting Information). We substitute this substrate temperature data, $T(t)$ into the Arrhenius expression for the crystallization rate on Si, $k_{Si}[T_{Si}(t)] = k_0 exp(-E_A/k_B T(t))$: Here, k_B is Boltzmann's constant, and we use the Arrhenius pre-factor k_0 and Arrhenius activation energy (E_A) obtained from the fit in Figure 4c since these constants should be independent of the substrate on account of the presence of the TPTPA underlayer between the rubrene and either SiN or glass.

Next, we integrate the growth rate as a function of time to yield the expected crystallization radius as a function of time on SiN (Figure 5, blue)

$$R_{Si}(t) = \int dt' \frac{dR_{Si}(t')}{dt'} = \int dt' k_{Si}\left[T_{Si}(t')\right] \quad (2)$$

Finally, we estimate the temperature range over which the platelet-to-spherulite transition occurs. To do so, we relate the onset radii obtained from STXM analysis (Table 1) to a corresponding SiN substrate temperature by matching the time window (as shown by guide arrows in Figure 5) at which films annealed on SiN are estimated to have the same range of crystallized radii (also Table 1). Despite the variation in the onset radius at which the platelet-to-spherulite transition occurs, the corresponding temperature is consistently ~135°C, where due to uncertainty in the onset radius and the timing of the Si chip measurement, this temperature can be specified no more than beyond the range from 122 to 146 °C. This estimate seems reasonable based on additional corroboration with the crystallized radii of films annealed on SiN windows for shorter durations (Figure S11, Supporting Information).

A commonly observed microstructure in our multimodal observations is the presence of a platelet-to-spherulite transition that our analysis suggests is due to finite substrate thermalization time. Hotplate annealing conditions are typically 140°C to crystallize platelet films, where rubrene molecules locally find their energetic single-crystal minimum through rotation, or 170°C to crystallize spherulites where molecules are not able to rotationally probe a sufficient number of configurations, which leads to polycrystalline branching.[19,24,25] Note that these temperatures are lower than the bulk crystallization temperature of 173°C, on account of decreased film thickness and finite surface effects.[19,26,27] We hypothesize that the finite substrate thermalization time of the film with the hotplate leads to the observed platelet-to-spherulite transition. A sufficient amount of time is first spent at platelet-forming temperatures before spherulite-forming temperatures are attained.

The hybrid microstructure is seen in both polarized STXM and 4D-STEM at different scales and in different spherulites annealed for different amounts of time. Notably, the rubrene thin films measured in 4D-STEM were annealed for ~5 s due to the extreme 10 nm thinness of the SiN membrane used (Figure S11, Supporting Information). Thicker SiN membranes such as those used in the STXM measurements (100–200 nm), required longer annealing times, e.g., 1 min., to obtain complete crystalline coverage, though the greater thickness likely serves to delay the onset of crystallization after which the dynamics proceed similarly to those of the thinner membranes. We suspect that the different thicknesses of SiN membranes both spend ~3–4.5 s in the platelet-forming temperature regime based on the Si temperature rise (Figure 5, orange). Although as little as 5 s are spent annealing on the hotplate, we propose that when the SiN membrane is taken off it, the substrate is effectively insulated by the surrounding air, so that crystallization may continue for some time afterward and lead to continuing growth of the spherulite microstructure for films annealed for less than a minute. Based on our observations and calculations, a hybrid microstructure likely occurs somewhat universally despite different annealing times and substrate parameters, due to the finite substrate equilibration time taken to achieve the desired annealing temperature.

To investigate the presence of hybrid microstructures induced by non-isothermal processing conditions more readily in organic semiconductors other than rubrene, we chose to use POM since it is readily accessible in a processing lab. Because POM does not have the same high resolution of STXM and 4D-STEM that we made use of to discover and characterize the hybrid rubrene structure in detail, we instead elected to thermally anneal two other organic semiconductor films by deliberately more slowly controlling the annealing temperature rise versus time. The complete protocol descriptions are included in the Materials and Methods. **Figure 6** shows POM of films of (±)-2,2″-bis(diphenylphosphino)-1,1″-binaphthyl (rac-BINAP) and 3,4,5,6-tetrakis(carbazol-9-yl)-1,2-dicyanobenzene (4CzPN) on glass/ITO substrates annealed following this process. Similar to rubrene, rac-BINAP (Figure 6a) shows single-crystalline platelet domains surrounding a common central nucleus, each indicated by a different, extended, uniform color under crossed-polarizers. The platelets give way to spherulite morphology ~250 µm from the nucleus, characterized by a more gradual azimuthal change in color indicating a gradual change in crystal orientation. The areas most similar to our rubrene observations are enclosed by red boxes, although there are gradual crystal orientation changes throughout the entire azimuthal range adjacent to any given platelet domain; one difference relative to our rubrene observation is that the relationship between spherulite-like regions that emerge from one platelet domain and others in rac-BINAP show more intervening orientational discontinuities. This could be a result of the specific details of the protocols, and employing a lower initial temperature to reduce the number of platelet domains might have yielded even more similar hybrid microstructures to the rubrene ones. For 4CzPN (Figure 6b), similar motifs to rac-BINAP are observed in some areas, as indicated by the red arc "underlining" the location of change between platelet and spherulite regions ~100 µm from the common platelet

 © 2023 Wiley-VCH GmbH

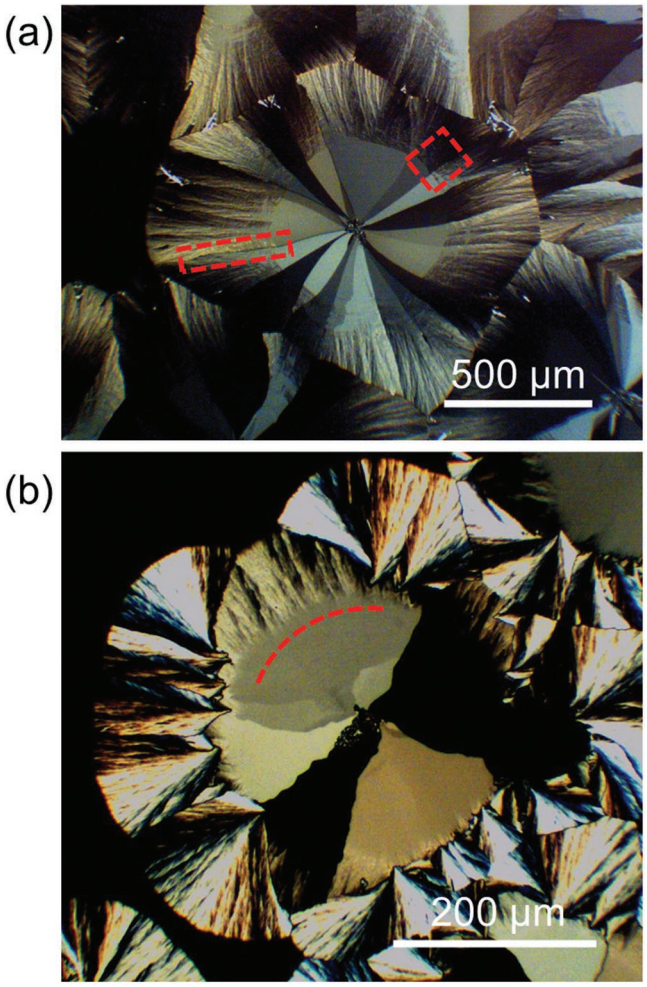

Figure 6. Observation of hybrid microstructures in additional organic semiconductor thin films. a) POM of rac-BINAP film on glass/ITO, where the red boxes highlight examples of a platelet-to-spherulite transition similar to rubrene. b) 4CzPN film on glass/ITO where the red arc guides the eye to observe the area of transition from platelet-like morphology to spherulite-like at slightly larger radius from the platelets' common nucleus.

nucleus. Also in 4CzPN, we observe the possibility for multiple incoherent spherulite nucleation events occurring at different azimuthal positions as yet another hybrid motif. If the heating during the annealing process were more rapid than what we were confident would be observable by POM, it is likely that similar structures observed in the rubrene films by STXM and 4D-STEM would also form. This investigation suggests that hybrid microstructures are indeed potentially more universal than what we discovered in our detailed investigation of rubrene and that their potential presence should be acknowledged when considering functional properties such as transporting organic semiconducting thin films.

More broadly, since organic semiconductor molecules are susceptible to polymorphism and multiple morphologies, it is important to both employ and understand the specific processing parameters that produce the desired crystal structure and morphology for optimal device performance. For example, previous research has shown that a high heating rate can bypass the triclinic phase of rubrene to preferentially crystallize orthorhombic platelet domains.[26] Here, we find a hybrid microstructure that is completely orthorhombic but that initially has a high-angle orientational discontinuity that disappears with elevated temperatures. While one might propose that a faster heating rate would circumvent the hybrid microstructure of a platelet transitioning into a spherulite, our observations remind us that achieving a uniform organic film is quite challenging, and a spectrum of morphologies or crystal structures often manifest. The organic molecule identity itself strongly determines the ease of uniformly producing a microstructure. If it is capable of forming both single-crystalline and polycrystalline structures, ideally the single-crystalline domains would form at lower temperatures to avoid complex processing or even modification strategies. Given that organic semiconductors easily form multiple morphologies that impact their resulting functionality in devices, characterizing organic thin films on multiple length scales provides a more complete understanding of heterogeneity in films.

Returning to a main theme of this work, multimodal imaging enables our observation of the hybrid microstructure in annealed rubrene thin films and the probable cause of its formation. As the macroscopic characterization technique, POM underpins our multimodal approach to quickly inspect whether we crystallized platelets or spherulites and to serve as a cross-reference for areas of interest before studying the films with other techniques. We learn about the rich nanoscale surface morphology of the films with AFM. Neither POM nor AFM, however, provides direct quantitative crystallite orientation of the thin films. The quantitative orientation information is instead obtained with polarized STXM and 4D-STEM in complementary ways. Polarized STXM provides micron-to-nanoscale features with variable sizes for fields-of-view from hundreds of microns to nanometers. The variable field-of-view sizes facilitated our ability to capture the disappearance of the orientational discontinuity. We use 4D-STEM to corroborate the polarized STXM images of the orientational discontinuity in the crystalline rubrene structure at high resolution and signal-to-noise ratio. To image these rubrene films using a focused scanning electron beam with 4D-STEM requires cryogenic conditions and recent advances in the TEM community.[16] Optimizing image acquisition parameters in X-ray and electron microscopies is clearly essential since organic films are often susceptible to damage from these radiation sources.[28] Finally, we connected these high-spatial resolution static images with in situ dynamic recordings of rubrene crystallization via POM, which is fully non-invasive and allows for in situ dynamical measurements of the annealing process beyond what is possible by examining the final product of the process. It is only through a multimodal imaging approach that allowed us to probe rubrene thin films on multiple length and time scales, that we were able to learn about how the finite substrate thermalization time leads to a platelet-spherulite hybrid microstructure. Furthermore, relating all observations requires not only cross-referencing across multiple scales but also across different substrates. The underlayer ensures that rubrene crystallization is consistent irrespective of whether we anneal on glass/ITO or SiN, since it ends up being the effective substrate for rubrene in both cases. This underlayer minimizes the

© 2023 Wiley-VCH GmbH

16163028, 2023, 13, Downloaded from https://onlinelibrary.wiley.com/doi/10.1002/adfm.202207867 by University Of Colorado Librari, Wiley Online Library on [09/06/2023]. See the Terms and Conditions (https://onlinelibrary.wiley.com/terms-and-conditions) on Wiley Online Library for rules of use; OA articles are governed by the applicable Creative Commons License

effects of surface roughness from glass/ITO, such that similar structures are formed atop of it and SiN.[19] This processing strategy also eliminates the need to transfer the film between substrates for different measurements. By incorporating a multimodal imaging approach that allowed us to probe rubrene thin films on multiple length scales, we learn about how the finite substrate thermalization time leads to a platelet-spherulite hybrid microstructure.

3. Conclusion

In sum, we combined optical, polarized X-ray, and electron microscopies to discover and characterize a hybrid microstructure in organic semiconductor thin films that emerges during thermal annealing. Polarized STXM and 4D-STEM of the annealed structures both demonstrate an orientational discontinuity emanating from a central nucleus and gradually disappearing toward its circular growth front. In situ POM of the crystallization process reveals Arrhenius crystallization behavior and measurement of substrate thermalization time allows us to map between time, temperature, and crystallization radius to determine the temperature at which the spherulite morphology develops. By combining POM, polarized STXM, and 4D-STEM, we determine that the finite substrate thermalization produces a hybrid microstructure because a non-negligible amount of annealing time is spent at a platelet-forming temperature before proceeding to spherulite crystallization temperatures. We furthermore illustrate how such hybrid microstructures can be formed in rac-BINAP and 4CzPN, indicating that rubrene is not anomalous in this regard.

In the future, hybrid structures could be designed deliberately to perform multiple functions, balancing high charge transport in platelet regions[19] with good charge transport isotropy in spherulite regions.[29] For example, if processing protocols were developed to maximize platelet domain area and introduce spherulite morphology at the growth front, one could overcome high-angle grain boundaries between separate platelet structures and still leverage the majority-platelet film charge carrier mobility while avoiding trapping. This protocol could be varied to optimize the overall needs of the film. A similar strategy could be used to enhance heterostructures between organic films and halide perovskite of transition metal dichalcogenides to overcome transport deficiencies in each[30–32] or to investigate thermoelectric applications.[33]

More generally as multimodal imaging opportunities continue to expand for organic materials such approaches may be used to capture in situ crystallization of additional films to elucidate understanding of spherulite formation or other crystalline microstructures. Multimodal imaging will surely advance to capture atomic and nanoscale in situ growth of crystals, which would be especially useful to elucidate spherulite formation. Specifically, for rubrene, the multimodal approach could be further leveraged to understand rubrene's inverted thermal spherulite growth behavior whereby spherulites occur at higher temperatures closer to the melting point. All of these possibilities speak to an exciting future for film characterization and processing as multimodal studies continue to increase in sophistication. Multimodal studies that incorporate measurements of function, such as transport, are clearly on the horizon.[34,35]

4. Experimental Section

The primary materials studied in this work include rubrene and tris(4-(5-phenylthiophen-2-yl)phenyl)amine (TPTPA), both of which were sourced from Lumtec. Rubrene was purified via thermal gradient sublimation prior to use. All samples were prepared following Fusella et al.[19] All glass/ITO substrates were cleaned successively by sonication in deionized water with Extran soap in a 6:1 ratio, deionized water, acetone, and isopropanol followed by an oxygen plasma treatment. The silicon nitride (SiN) membranes were cleaned only by an oxygen plasma treatment before use. Samples were deposited using thermal evaporation with a base pressure of ~10^{-7} Torr. To form rubrene films 40 nm of rubrene was deposited after depositing 5 nm of TPTPA. The annealing step was completed by placing the samples directly on a preheated hotplate in a nitrogen-filled glovebox. To target spherulite growth the films on glass/ITO substrates were annealed at 170 °C for 10 s^{-2} min, depending on the extent of crystallization desired, while those deposited on SiN windows on 200 µm Si frames (Norcada) were annealed at 170 °C for 5 s^{-1} min, depending on the extent of crystallization desired and on the thickness of the SiN. Control films annealed to form predominantly platelets were annealed at 140 °C for 1 min on glass/ITO or 45 s – 5 min on the SiN substrates.

Additional characterization of organic semiconductor materials were (±)-2,2″-bis(diphenylphosphino)-1,1″-binaphthyl (rac-BINAP) and 3,4,5,6-tetrakis(carbazol-9-yl)-1,2-dicyanobenzene (4CzPN), which were sourced from Alfa Aesar and Xi'an Polymer Light Technology Corp., respectively. Glass/ITO substrates were cleaned as described above. Samples were deposited using thermal evaporation with a base pressure of 10^{-6} Torr. To form rac-BINAP and 4CzPN films, 60 nm of both rac-BINAP and 4CzPN were deposited directly onto the glass/ITO substrates. rac-BINAP films were annealed at 153 °C for 3 min followed by 155 °C for 30 s. The 4CzPN films were placed on a preheated hotplate set to 180 C, and the temperature was immediately decreased to 155 °C for a total annealing time of 5 min.

AFM: AFM imaging was performed in tapping mode with an Asylum MFP-3D with TAP 150 AL silicon AFM probes (Ted Pella, Inc.). For the images shown in the main text, the scans were collected with a 583 mV setpoint and a 2.5–2.6 V amplitude. Figure 1d has a 29.2 nm per pixel resolution with a 0.75 Hz scan rate, and Figure 1e had a 19.6 nm per pixel resolution with a 0.5 Hz scan rate. The sample imaged by AFM was annealed for 5 s at 170 °C on 10 nm of SiN (NT050Z).

STXM: All X-ray microscopy measurements were performed at the 11.0.2.2 beamline at the Advanced Light Source at the Lawrence Berkeley National Laboratory, California. Figure 2a,b were annealed at 170 °C for 1 min on a SiN window with an area of 1.5 × 1.5 mm2 and 200 nm in thickness that is mounted on a 5 × 5 mm2 Si frame with 200 µm thickness (NX5150D). Control films were annealed at 140 °C for 5 min on a SiN window with an area of 1 × 1 mm^2 and a 100 nm thickness (NX5100C). The film used to generate the NEXAFS spectrum (Figure S4, Supporting Information) was annealed at 170 °C for 5 s on a SiN window with an area of 2 × 2 mm^2 and 200 nm thickness (NX5200D). Samples were mounted onto an aluminum plate inside of the sample chamber that was evacuated to ~30 mTorr and refilled with 200 Torr of helium. A NEXAFS spectrum (Figure S4, Supporting Information) and identified energies with linear dichroic contrast at 284.5, 285.3, and 286.1 eV were collected. Each image was collected at both vertical and horizontal polarizations at 284.5 eV because of its strong dichroic contrast.

Image viewing and analysis was facilitated by the IDL program aXis2000 from the Hitchcock Group at McMaster University and the STXM Data Analysis Matlab script collection from T.R. Henn (Physikalisches Institut, Germany) and R.C. Moffet (Lawrence Berkeley National Laboratory, USA). Transmission intensity radial profiles were generated with singly polarized images by first identifying the pixel

© 2023 Wiley-VCH GmbH

16163028, 2023, 13, Downloaded from https://onlinelibrary.wiley.com/doi/10.1002/adfm.202207867 by University Of Colorado Librari, Wiley Online Library on [09/06/2023]. See the Terms and Conditions (https://onlinelibrary.wiley.com/terms-and-conditions) on Wiley Online Library for rules of use; OA articles are governed by the applicable Creative Commons License

coordinates of $r = 0$ µm corresponding with the nucleus with Fiji.[36] To calculate the average pixel intensity at a given radius, pixel intensities were collected that fall within a user-defined radial width (Figure S5, Supporting Information) and bin them in increments of 1° from 1° to 360°.

Data shown in the main text (Figure 2c,d) use a radial width of 4.5 µm that corresponds with ~10 pixels per bin. The average pixel intensity and corresponding standard deviation were calculated for each bin and represent one average intensity datapoint at a single radius.

This protocol was repeated to plot average pixel intensity as a function of radius from the center of the spherulite and outward from it as shown in Figure 2c,d in the main text. Due to poor signal-to-noise close to the nucleus, plotting the average pixel intensity at 20 µm was started.

The transmission intensity radial profiles were fitted to the piecewise function described by Equation 1 in the main text. The maximum and minimum intensity of a spherulitic azimuthal transmission intensity profile were used to convert intensity values into approximate crystal orientation as described in the main text and in the Supporting Information with Figure S6 (Supporting Information).

4D-STEM: 4D-STEM data were acquired using a ThermoFisher Scientific ThemIS transmission electron microscope operated at 300 kV accelerating voltage. During imaging, the sample was cooled to ~90 K by a Gatan 636 cryo holder. The 4D-STEM datasets were acquired with a probe semiconvergence angle of 0.59 mrad across a grid of 512 × 512 pixels, with a step size of 15.5 nm between probe positions. For rapid acquisition of large-area maps with minimal sample drift, the microscope was fitted with an IDES Relativity electrostatic subframing system. This system divides the detector frame into multiple subframes and rapidly deflects the diffraction pattern into each frame as the beam steps to different probe positions, allowing multiple diffraction patterns to be acquired per readout of the detector. Datasets were acquired with a probe dwell time of 2.24 ms, a 4 × 4 grid of subframes, and a detector exposure time of 36 ms.

All analysis of the 4D-STEM datasets was performed using py4DSTEM, an open-source Python package.[15,22] In order to produce the orientation maps, the template cross correlation method was first used to locate the positions of each of the diffraction disks in each diffraction pattern. These Bragg disk locations were then calibrated to remove any elliptical distortion caused by the microscope, artifacts caused by translations of the diffraction pattern, and to correct the pixel size. Using the Automated Crystal Orientation Matching (ACOM) submodule of py4DSTEM, a library of simulated rubrene diffraction peaks was generated using the known orthorhombic crystal structure. As it is known that the films were primarily oriented with the *c* axis normal to the substrate, patterns with up to 5° mistilt were only simulated from this orientation. The ACOM matching algorithm compares each experimental list of Bragg disk locations to the simulations and finds the best match zone axis, along with the in-plane orientation of the crystal.

POM: Static and dynamic POM measurements were performed with a Nikon Eclipse LV100ND in EPI mode. Images and videos were taken with an Infinity 2 Lumenera camera and Infinity Analyze and Infinity Capture software. For in situ annealing measurements, to assist in quickly finding the appropriate focal plane, a fiducial was marked on amorphous rubrene samples on glass/ITO substrates in a nitrogen-filled glovebox. The films were encapsulated with UV-curing epoxy from EPO-TEK (OG116-31) using a coverslip (Fisher 12-541-B) cleaned in acetone, 2-propanol, and Millipore water after that the encapsulated films were removed from the glovebox. A Thorlabs HT24S metal ceramic heater was placed underneath the Nikon Tu Plan Fluor 10x objective in the microscope and layered with thermally conductive materials described in the Supporting Information. The ceramic heater temperature was regulated by a Thorlabs TC200 temperature controller and the auxiliary port was connected to a Thorlabs TH100PT thermistor that monitored the surface temperature of the thermal pad atop of the annealing configuration shown in Figure S9 (Supporting Information). The microscope settings were recorded for this focal plane. The Thorlabs TC200 was set to the desired temperature setpoint. The ceramic heater temperature was allowed to stabilize for a minimum of 2 min before beginning to record video. The sample was quickly placed onto the annealing setup, and minor adjustments to the focus were made using the fiducial, which had been used to focus the imaging system prior to heating. The crystallization process was imaged at a rate of 11 frames per second, and the sample was removed once the field of view captured in the video was completely crystalline.

Tracking the radial growth of spherulites in POM videos was done in Fiji with a custom macro applied to the video in the form of an image stack. The images were binarized based on crystalline and amorphous rubrene distinction with the centroid, perimeter, and area recorded for each circular feature in a given image. Then the images were background subtracted for processing in a custom Jupyter notebook to calculate the average radius of the circular features in each frame.

Supporting Information

Supporting Information is available from the Wiley Online Library or from the author.

Acknowledgements

The authors thank J. Utterback for helpful heat transport discussions. The authors thank C. Zhu for valuable discussion on GIWAXS interpretation and analysis. The authors also thank H.-G. Steinrück for advice on the Scherrer analysis. The authors thank M. Marcus for guidance on preliminary STXM measurements at the 5.3.2.2 beamline at the Advanced Light Source at the Lawrence Berkeley National Laboratory. STXM, POM, 4D-STEM, GIWAXS, IR *s*-SNOM, and AFM and subsequent analysis had been supported by STROBE, A National Science Foundation Science & Technology Center under Grant No. DMR 1548924. The TEM imaging at the Molecular Foundry was supported by the Office of Science, Office of Basic Energy Sciences, of the U.S. Department of Energy under Contract No. DE-AC02-05CH11231. GIWAXS, SINS, and STXM were performed as part of the Advanced Light Source user program, supported by the Office of Science, Office of Basic Energy Sciences, of the U.S. Department of Energy under Contract No. DE-AC02-05CH11231. J. A. T. acknowledges a National Defense Science and Engineering Graduate Fellowship, and N.S.G. acknowledges an Alfred P. Sloan Research Fellowship, a David and Lucile Packard Foundation Fellowship for Science and Engineering, and a Camille and Henry Dreyfus Teacher-Scholar Award. J.T.D. and B.P.R. acknowledge support from a Princeton SEAS Project X award.

Conflict of Interest

The authors declare no conflict of interest.

Data Availability Statement

The data that support the findings of this study are available from the corresponding author upon reasonable request.

Keywords

crystallization, microstructures, morphology, multiscale/multimodal imaging, thin films

Received: July 10, 2022
Revised: December 20, 2022
Published online: January 19, 2023

© 2023 Wiley-VCH GmbH

16163028, 2023, 13, Downloaded from https://onlinelibrary.wiley.com/doi/10.1002/adfm.202207867 by University Of Colorado Librari, Wiley Online Library on [09/06/2023]. See the Terms and Conditions (https://onlinelibrary.wiley.com/terms-and-conditions) on Wiley Online Library for rules of use; OA articles are governed by the applicable Creative Commons License

[1] A. L. Foggiatto, Y. Takeichi, K. Ono, H. Suga, Y. Takahashi, M. A. Fusella, J. T. Dull, B. P. Rand, K. Kutsukake, T. Sakurai, *Org. Electron.* **2019**, *74*, 315.
[2] S. S. Lee, J. M. Mativetsky, M. A. Loth, J. E. Anthony, Y. - L. Loo, *ACS Nano* **2012**, *6*, 9879.
[3] A. K. Hailey, S. - Y. Wang, Y. Chen, M. M. Payne, J. E. Anthony, V. Podzorov, Y. - L. Loo, *Adv. Funct. Mater.* **2015**, *25*, 5662.
[4] A. A. Virkar, S. Mannsfeld, Z. Bao, N. Stingelin, *Adv. Mater.* **2010**, *22*, 3857.
[5] A. M. Hiszpanski, P. P. Khlyabich, Y. - L. Loo, *MRS Commun.* **2015**, *5*, 407.
[6] V. Podzorov, E. Menard, A. Borissov, V. Kiryukhin, J. A. Rogers, M. E. Gershenson, *Phys. Rev. Lett.* **2004**, *93*, 086602.
[7] J. E. Anthony, *Chem. Rev.* **2006**, *106*, 5028.
[8] A. Salleo, R. J. Kline, D. M. DeLongchamp, M. L. Chabinyc, *Adv. Mater.* **2010**, *22*, 3812.
[9] C. Groves, O. G. Reid, D. S. Ginger, *Acc. Chem. Res.* **2010**, *43*, 612.
[10] A. P. Hitchcock, *J Synchrotron Rad* **2001**, *8*, 66.
[11] J. Eichhorn, S. E. Reyes-Lillo, S. Roychoudhury, S. Sallis, J. Weis, D. M. Larson, J. K. Cooper, I. D. Sharp, D. Prendergast, F. M. Toma, *Small* **2020**, *16*, 2001600.
[12] B. A. Collins, H. Ade, *J. Electron Spectrosc. Relat. Phenom.* **2012**, *185*, 119.
[13] C. R. McNeill, B. Watts, L. Thomsen, H. Ade, N. C. Greenham, P. C. X.-R. Dastoor, *Macromolecules* **2007**, *40*, 3263.
[14] Y. Wen, Y. Liu, Y. Guo, G. Yu, W. Hu, *Chem. Rev.* **2011**, *111*, 3358.
[15] C. Ophus, S. E. Zeltmann, A. Bruefach, A. Rakowski, B. H. Savitzky, A. M. Minor, M. C. Scott, *Microsc. Microanal.* **2022**, *390*.
[16] K. C. Bustillo, S. E. Zeltmann, M. Chen, J. Donohue, J. Ciston, C. Ophus, A. M. Minor, *Acc. Chem. Res.* **2021**, *54*, 2543.
[17] O. Panova, C. Ophus, C. J. Takacs, K. C. Bustillo, L. Balhorn, A. Salleo, N. Balsara, A. M. Minor, *Nat. Mater.* **2019**, *18*, 860.
[18] A. Belianinov, A. V. Ievlev, M. Lorenz, N. Borodinov, B. Doughty, S. V. Kalinin, F. M. Fernández, O. S. Ovchinnikova, *ACS Nano* **2018**, *12*, 11798.
[19] M. A. Fusella, S. Yang, K. Abbasi, H. H. Choi, Z. Yao, V. Podzorov, A. Avishai, B. P. Rand, *Chem. Mater.* **2017**, *29*, 6666.
[20] T. R. Fielitz, R. J. Holmes, *Cryst. Growth Des.* **2016**, *16*, 4720.
[21] S. A. Dönges, R. P. Cline, S. E. Zeltmann, J. Nishida, B. Metzger, A. M. Minor, J. D. Eaves, M. B. Raschke, *Nano Lett.* **2021**, *21*, 6463.
[22] B. H. Savitzky, S. E. Zeltmann, L. A. Hughes, H. G. Brown, S. Zhao, P. M. Pelz, T. C. Pekin, E. S. Barnard, J. Donohue, L. R. DaCosta, E. Kennedy, Y. Xie, M. T. Janish, M. M. Schneider, P. Herring, C. Gopal, A. Anapolsky, R. Dhall, K. C. Bustillo, P. Ercius, M. C. Scott, J. Ciston, A. M. Minor, C. Ophus, *Microscopy and Microanalysis* **2021**, *27*, 712.
[23] S. - W. Park, J. - M. Choi, K. H. Lee, H. W. Yeom, S. Im, Y. K. Lee, *J. Phys. Chem. B* **2010**, *114*, 5661.
[24] A. G. Shtukenberg, Y. O. Punin, E. Gunn, B. S. Kahr, *Chem. Rev.* **2012**, *112*, 1805.
[25] L. Gránásy, T. Pusztai, G. Tegze, J. A. Warren, J. F. Douglas, *Phys. Rev. E* **2005**, *72*, 011605.
[26] P. C. Jukes, A. Das, M. Durell, D. Trolley, A. M. Higgins, M. Geoghegan, J. E. Macdonald, R. A. L. Jones, S. Brown, P. Thompson, *Macromolecules* **2005**, *38*, 2315.
[27] J. H. Kim, J. Jang, W. - C. Zin, *Macromol. Rapid Commun.* **2001**, *22*, 386.
[28] J. Rivnay, S. C. B. Mannsfeld, C. E. Miller, A. Salleo, M. F. Toney, *Chem. Rev.* **2012**, *112*, 5488.
[29] S. S. Lee, M. A. Loth, Anthony, Y.-L. Loo, *J. Am. Chem. Soc.* **2012**, *134*, 5436.
[30] C. - J. Park, H. J. Park, J. Y. Lee, J. Kim, C. - H. Lee, J. Joo, *ACS Appl. Mater. Interfaces* **2018**, *10*, 29848.
[31] F. Liu, W. L. Chow, X. He, P. Hu, S. Zheng, X. Wang, J. Zhou, Q. Fu, W. Fu, P. Yu, Q. Zeng, H. J. Fan, B. K. Tay, C. Kloc, Z. V. Liu, *Adv. Funct. Mater.* **2015**, *25*, 5865.
[32] D. Jariwala, T. J. Marks, M. C. Hersam, *Nature Mater* **2017**, *16*, 170.
[33] B. Russ, A. Glaudell, J. J. Urban, M. L. Chabinyc, R. A. Segalman, *Nat. Rev. Mater.* **2016**, *1*, 1.
[34] N. S. Ginsberg, W. A. Tisdale, *Annu. Rev. Phys. Chem.* **2020**, *71*, 1.
[35] Z. Guo, Y. Wan, M. Yang, J. Snaider, K. Zhu, L. Huang, *Science* **2017**, *356*, 59.
[36] J. Schindelin, I. Arganda-Carreras, E. Frise, V. Kaynig, M. Longair, T. Pietzsch, S. Preibisch, C. Rueden, S. Saalfeld, B. Schmid, J. - Y. Tinevez, D. J. White, V. Hartenstein, K. Eliceiri, P. Tomancak, A. F. Cardona, *Nat. Methods* **2012**, *9*, 676.

© 2023 Wiley-VCH GmbH

16163028, 2023, 13, Downloaded from https://onlinelibrary.wiley.com/doi/10.1002/adfm.202207867 by University Of Colorado Librari, Wiley Online Library on [09/06/2023]. See the Terms and Conditions (https://onlinelibrary.wiley.com/terms-and-conditions) on Wiley Online Library for rules of use; OA articles are governed by the applicable Creative Commons License